

Title	Spatial mode dynamics in wide-aperture quantum-dot lasers
Authors	Mukherjee, Jayanta;McInerney, John G.
Publication date	2009
Original Citation	Mukherjee, J. and McInerney, J. G. (2009) 'Spatial mode dynamics in wide-aperture quantum-dot lasers', Physical Review A, 79(5), 053813 (15pp). doi: 10.1103/PhysRevA.79.053813
Type of publication	Article (peer-reviewed)
Link to publisher's version	https://journals.aps.org/pr/abstract/10.1103/PhysRevA.79.053813 - 10.1103/PhysRevA.79.053813
Rights	© 2009, American Physical Society
Download date	2024-04-25 17:37:13
Item downloaded from	https://hdl.handle.net/10468/4536



UCC

University College Cork, Ireland
 Coláiste na hOllscoile Corcaigh

Spatial mode dynamics in wide-aperture quantum-dot lasers

Jayanta Mukherjee and John G. McInerney

Department of Physics and Tyndall National Institute, Optoelectronics Group, National University of Ireland, University College, Cork, Ireland

(Received 18 September 2008; published 6 May 2009)

We present a systematic theoretical study of spatial mode dynamics in wide-aperture semiconductor quantum-dot lasers within the Maxwell-Bloch formalism. Our opto-electro-thermal model self-consistently captures the essential dynamical coupling between field, polarization, and carrier density in both thermal and nonthermal regimes, providing detailed description of the complex spatiotemporal modal intensity structure and spectra in these novel devices and broad area edge-emitting lasers in general. Using linear stability analysis and high resolution adaptive-grid finite element numerical simulation, we show that in the nonthermal regime, the presence of inhomogeneous broadening in quantum-dot active media leads to suppressed filamentation and enhanced spatial coherence compared to conventional quantum well devices with comparable phase-amplitude coupling (α parameter). Increasing the degree of inhomogeneous broadening in the active medium leads to further improvement in spatial coherence. In the thermal regime, there is further suppression of filamentation in the inhomogeneously broadened quantum-dot active medium; however, the spatial coherence aided by inhomogeneous broadening is partly lost due to the effect of temperature on cavity detuning. We propose that device designs based on optimized inhomogeneous broadening of quantum-dot gain medium could ultimately lead to diffraction-limited outputs in the quasi-cw regime which are still very difficult to achieve in conventional wide-aperture designs.

DOI: [10.1103/PhysRevA.79.053813](https://doi.org/10.1103/PhysRevA.79.053813)

PACS number(s): 42.55.Px, 42.60.Mi, 42.65.Sf

I. INTRODUCTION

Design and technology of semiconductor lasers has come a long way since their advent in the early 1960s, and as a result, these lasers have revolutionized communication, data, and material processing. Semiconductor lasers are preferred over gas and solid-state lasers due to their wide tuning range, high wall plug efficiency, compactness, and reliability. While low-power diode lasers are used in communication and data processing, their high-power counterparts find use in modern medical and surgical equipment, material processing, and optical pumping of solid-state lasers. Tremendous advancements have been made in scaling the output power of diode lasers and arrays, thanks to modern crystal growth, device cooling, and facet passivation technologies. Over the last two decades the output power from diode lasers has increased by an order of magnitude [1]. However, several issues still remain as open challenges. An important issue of achieving high brightness, requiring production of good output beam quality and narrow optical spectra from high-power diode lasers, is still far from what is achievable from solid-state and gas lasers. High brightness, high-power diode laser sources are gaining more and more interest for applications previously dominated by solid-state lasers, because of their efficiency, compactness, and high reliability. Among others, laser projection displays, free-space communication, frequency doubling, and direct material processing are rapidly emerging areas, where high output power together with diffraction-limited beam quality are either the key requirements or strongly enhance system performance. Production of high-power diode lasers with improved brightness will allow them to compete with the very best solid-state and gas lasers at much lower cost [2–4], and may enable future generations of compact, inexpensive, and portable laser systems.

High-power semiconductor lasers require wide-aperture designs to achieve the necessary gain and efficient heat dissipation under cw operation [2,3]. But these devices are plagued by modal instabilities and filamentation which severely reduce their brightness (focusing) and output-coupling properties. Filamentation and self-focusing of high intensity laser beams propagating in a nonlinear medium has been a topic of extensive investigation from the early days of high-power solid-state and gas lasers [5–7], occurring when the refractive index of the medium responds nonlinearly to strong laser beams and/or pumping. The nonlinearity can be Kerr-type, ponderomotive, relativistic mass nonlinearity, Ohmic heating or other type, but the mechanism is believed to be similar: self-focusing balanced by diffraction [8]. High intensity portions of the laser wave front move into local refractive index peaks and travel with slower phase velocity, whereas lower intensity portions travel faster giving rise to wave front curvature hence focusing the beam toward the intensity maxima. This phenomenon is frequently observed in high-power laser-plasma interactions [9] and propagation of laser beams in the atmosphere [10]. Filamentation in wide-aperture semiconductor lasers has similarly been a long standing problem [11,12] and is generally described as a complex spatiotemporal instability of the higher-order spatial modes sustained in these devices. The mechanism is believed to be via carrier induced antiguiding, however, a complete picture of its origin and mechanism has yet to be revealed. Several designs have been proposed to alleviate this problem, but most have either been far too complex for practical realization or have failed to deliver the expected results at higher operating powers [13,14].

Not long after the first theories for quantum-dot (QD) lasers were outlined, it was realized that these devices have great potential for high-power and high brightness applications. Along with low threshold current densities, broad

spectral gain profiles and inhibited in-plane carrier diffusion, quantum-dot lasers are expected to have reduced values of phase-amplitude coupling (or alpha) parameter [15,16], which drives self-focusing in the media. While the low lasing threshold and reduced in-plane carrier diffusion raises the facet damage threshold under high-power operation [15], weak phase-amplitude coupling helps in suppressing filamentation thereby increasing spatial coherence of the output beam. Weak phase-amplitude coupling also makes QD lasers less susceptible to optical feedback [17], a property extremely beneficial while coupling the laser output into an optical fiber or other optical systems. It is a consequence of the atom (delta-function) like density of states in QD lasers that renders the gain response nearly symmetric, giving rise to a weak (ideally zero [18,19]) phase-amplitude coupling. Deviation from ideal behavior and experimental observation of nonzero alpha parameter has been attributed to many-body effects [20], inhomogeneous broadening [21], and free carrier plasma effect [19,22]. The broad gain profile in QD lasers is a consequence of size and shape fluctuation induced inhomogeneous broadening, which makes them suitable for mode locking and broadband operation [15].

A hierarchy of theoretical models and numerous experimental results exist in the literature analyzing the occurrence and mechanisms of filamentation in conventional double heterostructure (DH) and quantum well (QW) semiconductor lasers [2–4,11,12,23–25]. In comparison there are very few reports on filamentation properties in wide-aperture QD lasers [20]. It is generally believed that relatively high values (2–5) of the alpha parameter in conventional semiconductor lasers, in comparison to QD lasers (<2), causes or exacerbates this field instability. It has also been suggested that refractive index steps at the edges of the lateral pump profile can act as a destabilizing element for the spatial modes both by seeding filamentation and reflecting the lateral waves [26]. Thermal effects can also play a key role [27] in stabilizing (via thermal wave guiding) [28,29] or destabilizing (via self-focusing and beam steering at local hot spots) [29] the spatial mode structure. Surprisingly, there has been very limited study of such thermal effects in the available literature [4].

Much of our early theoretical understanding of filamentation in diode lasers has come from steady-state analysis of scalar the Helmholtz equation coupled to a carrier diffusion equation in the active layer [29–32]. However, in a seminal paper by Jakobsen *et al.* [33], it was shown that such a steady-state analysis can give ambiguous results leading to an erroneous interpretation of the mechanism and origin of filamentation [25]. The roots of this error can be traced back to the adiabatic elimination of material polarization dynamics. It is worth noting here that adiabatic elimination of material polarization forms the basis of the Lamb theory of laser [34–36], and hence has been considered an appropriate approximation historically. The material polarization is a fast-relaxing variable in comparison to the field and inversion, but its adiabatic elimination is only justified when spatial effects are not explicitly considered [37]. The presence of field diffraction allows the spatial wave numbers to evolve on a time scale comparable to inverse of the polarization decay rate, invalidating adiabatic elimination. A steady-state

model also renders the gain spectrum flat causing high wave-number instabilities on the same spatial scale as the spatial grid used to analyze field dynamics [37]. This calls for a model which incorporates the essential features required to describe a wide-aperture diode laser with sufficient accuracy without necessarily resorting to highly sophisticated models based on many-body physics which require extremely high computational power [38,39]. As described below, our model is equally capable of incorporating the gain and dispersion accurately allowing proper description of modal behavior in the laser. Moreover, we have self-consistently included the effect of junction temperature rise which is extremely difficult to incorporate in models based on many-body physics.

Experimental near- and far-field profiles from wide-aperture QD laser diodes under cw operation show marked improvement in spatial coherence over their QW counterparts [40]. In the past this has been mainly attributed to the weak phase-amplitude coupling found in QD lasers [40]. However, as we show below, inhomogeneous broadening in the QD gain medium can also play a very important role in deciding and improving the coherence properties, even when the phase-amplitude coupling is comparable to QW lasers. This prompts discussion as to why wide-aperture QD lasers show better beam quality than their QW counterparts and the relative importance of gain media broadening mechanism. As comparable values of α are frequently measured for both QW and QD lasers [41], investigation of the effects of line broadening on spatial mode structure and dynamics can have important and rewarding consequences. On the other hand, as we go to higher operating points, we find that the improved spatial coherence due to inhomogeneous broadening deteriorates, indicating possible deleterious influence from thermal effects. We therefore believe that only sophisticated numerical modeling, including thermal effects, can give us the required insight into the mechanism of filamentation in these novel devices, opening up possibilities to counter filamentation and eventually achieve filament free operation of high-power semiconductor lasers.

In this work, we address the problem of filamentation theoretically within the framework of Maxwell-Bloch equations for an edge-emitting wide-aperture semiconductor laser with a single active layer of QD's, systematically analyzing the effects of phase-amplitude coupling, junction temperature, and inhomogeneous broadening in the QD active layer on the spatial mode structure and dynamics. More specifically, we model within the mean-field formulation of the Maxwell-Bloch equations [42], where we track the spatial mode dynamics corresponding of a single longitudinal mode and assume negligible effect of interlongitudinal mode interaction on the spatial mode structure. This is justified as the interlongitudinal mode optical frequency spacing in these lasers is at least an order of magnitude greater than between adjacent spatial (lateral) modes. Thus the contribution of interlongitudinal mode interaction on spatial mode structure and dynamics is known to be weak [45]. Furthermore, for gain media such as quantum dots, interlongitudinal mode interaction is expected to be even weaker, as in the presence of inhomogeneous broadening different longitudinal modes are likely to extract gain from different sized dots so that the usual cross-gain saturation is unlikely [15,16].

The time scales involved in the dynamics of material polarization (\sim fs), field (\sim ps), and carriers (\sim ns) are much faster than the thermal time constant ($\sim\mu$ s) in semiconductor lasers. This essentially means that all the other variables see a constant temperature as they evolve in time. Thus we work within a window where we assume that the material polarization, field and carrier dynamics take place under a constant junction temperature when the laser is driven continuously. Temperature-induced index changes are included through the effective index in the field equation. Temperature dependences of parameters have been considered only where they are likely to effect the spatial mode selection, dynamics, and stability.

The remainder of the paper is organized as follows. In Sec. II we present the Maxwell-Bloch equations used in our analysis and outline the electrothermal model employed to obtain the junction current and temperature profiles. Linear stability analysis of the Maxwell-Bloch equations is discussed in Sec. III, where we examine the influence of various parameters: phase-amplitude coupling, junction temperature, and inhomogeneous broadening on the selection on spatial modes at the onset of lasing. Analysis beyond threshold requires numerical techniques to solve the coupled set of opto-electro-thermal equations, which we describe in Sec. IV along with the results. Finally we conclude in Sec. V with a summary of our work.

II. MAXWELL-BLOCH MODEL

Semiclassical quasi-two-level Maxwell-Bloch equations for a Fabry-Pérot inhomogeneously broadened semiconductor laser under mean-field, effective-index, rotating-wave, and slowly varying envelope approximations can be written as follows [46–48]:

$$\partial_t E = -\kappa_E [1 - i\delta_n^T(x)]E + iA\partial_x^2 E + \int_{-\infty}^{\infty} \tilde{g}(\theta)P(\theta)d\theta, \quad (1)$$

$$\partial_t P = \gamma_P \Gamma(N(\theta)) [1 + i\Delta^T(\theta)] \left[\frac{1}{2}(1 - i\alpha)g(N(\theta))E - P(\theta) \right], \quad (2)$$

$$\partial_t N = \Lambda(x) - \gamma_N N(\theta) + D\partial_x^2 N(\theta) - \frac{1}{2}[EP^*(\theta) + E^*P(\theta)], \quad (3)$$

where the effect of junction temperature on lateral (x -axis) refractive index and peak gain is also included.

The above equations are quasi-two-level because, unlike conventional two-level Maxwell-Bloch equations which are applicable strictly only to gas lasers [49,55], these equations completely describe the gain and dispersion in a generic semiconductor laser [48] with either homogeneously or inhomogeneously broadened active media. This is achieved by deviating from the conventional derivation and usage [48] of the polarization Eq. (2) in Maxwell-Bloch formalism as described in detail below. For two-level systems such as gaseous active media, the gain is symmetric and the dispersion

vanishes at the gain peak nullifying phase-amplitude coupling. Such a laser can be forced to operate away from the gain peak by detuning the cavity [50,51], but this detuning is generally an order of magnitude smaller than the alpha parameter. Putting cavity detuning as the alpha parameter has been a convenient choice for many authors over the years [37,52–54], simply because adiabatic elimination of polarization directly connects cavity detuning to the alpha parameter through its definition [54]. But, as pointed out by Martín-Regalado *et al.* [49], such an assumption is erroneous as it actually forces laser emission close to the gain peak. An alternative way to include the alpha parameter in Maxwell-Bloch equations is through carrier-dependent detuning in the field Eq. (1) [58,59]. But again this phenomenological approach lacks the true description of gain and dispersion in a semiconductor active medium, which as we will see later plays a very important role in deciding the spatial mode dynamics. Until now, only complicated and computationally expensive many-body physics based models [60] have been able to describe spatial mode dynamics in conventional semiconductor lasers with sufficient accuracy. No such study is available for QD lasers due to complications in the gain model [16]. The approach presented here relies on fitting carrier-dependent parameters in the polarization Eq. (2) to experimental gain and dispersion [48] within the quasiequilibrium approximation [60] and proves equally useful at much lower computational cost. At the same time, our model enables extraction of the physics behind the factors determining spatial mode structure in a wide-aperture QD laser. Also, our description self-consistently includes intensity-dependent gain saturation [48] and mode pulling [46] which otherwise can only be included phenomenologically in commonly used rate-equation description of semiconductor lasers. In earlier work, [61], wetting layer (WL) carrier dynamics was found to have very little effect on the spatial mode structure unless carrier diffusion in this layer was increased to drastically high and unphysical values. Thus we do not consider WL carrier diffusion capture-escape dynamics here. Only electron dynamics is considered in this work under the hypothesis that holes being faster follow the electron dynamics [62]. Although we study QD lasers in this work, Eqs. (1)–(3) are completely capable of describing bulk and QW lasers with equal accuracy.

The field Eq. (1) above is derived under an effective index approximation [3] applicable to edge-emitting lasers and is equivalent to the conventional field equation [46,63] for an inhomogeneously broadened Fabry-Pérot laser when temperature-induced effective-index perturbation (detuning) $\delta_n^T(x)$ is neglected. The carrier Eq. (3), which is in its conventional form [46], describes the spatiotemporal dynamics of the carriers N in a single active layer of quantum dots. E denotes TE polarized electric field describing the spatial modes and P is the material polarization. Both P and N are functions of the frequency detuning θ between the inhomogeneous line center and the line center of a homogeneous packet, see Fig. 1. θ is normalized to the polarization dephasing rate γ_P (half-width of each homogeneous packet). The inhomogeneous line shape is chosen as a Gaussian [64,65]

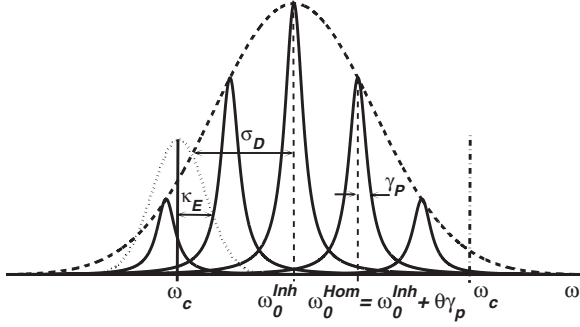


FIG. 1. Gain profile (Gaussian) for an inhomogeneously broadened QD medium. Individual Lorentzians of half-width γ_P corresponding to each homogeneous packet (QD's) at different resonant frequencies ω_0^{Hom} make the total line shape inhomogeneous. The inhomogeneous gain profile peak is centered at ω_0^{Inh} and its half-width is σ_D . Two cavity modes centered at ω_c are positioned at opposite sides of ω_0^{Inh} , both having a loss profile of half-width κ_E (not shown for the cavity mode above resonance for clarity). For $\Omega > 0$, the cavity mode at ω_c with solid line is the active mode. For $\Omega < 0$, cavity mode at the dot-dashed line is the active mode. Diagram is not to scale.

$$\tilde{g}(\theta) = \frac{1}{\sigma_D \sqrt{2\pi}} \exp\left(-\frac{\theta^2}{2\sigma_D^2}\right), \quad (4)$$

with half-width σ_D (also normalized to γ_P). The dimensionless detuning,

$$\delta_n^T(x) = \frac{\omega_c}{n_g \kappa_E} \delta n_T(x), \quad (5)$$

describes the effect of temperature-induced refractive index change $\delta n_T(x) = \beta_T T(x)$, where β_T denotes the temperature coefficient of refractive index and $T(x)$ is the lateral junction temperature (profile) above ambient. n_g is the group index and κ_E the field decay rate. The single mode cavity resonance frequency ω_c is chosen as the basis for deriving the Maxwell-Bloch equations [63]. $A = c^2 [2\omega_c n_e n_g]^{-1}$ is the diffraction parameter with n_e the effective index of refraction. Γ (normalized to γ_P) represents the carrier dependent broadening of the gain spectrum [60]. Γ is also temperature dependent and has a square root dependence on temperature for bulk GaAs lasers [66]. However, for a QD gain medium, the temperature dependence of Γ turns out to very weak for the temperature ranges encountered in this work (< 5 K) [67] and hence has been neglected in this work. $g(N(\theta)) = a_n [N(\theta) - N_{tr}]$ is the modal gain in the active medium, N_{tr} the transparency carrier density and a_n the modal differential gain. α is the phase-amplitude coupling or alpha parameter (also known as the linewidth enhancement factor) [2,57]. The modal differential gain $a_n \propto \sigma_{res} \Gamma_y c n_e^{-1}$, where

$$\sigma_{res} = \frac{2|\Phi|^2 \omega_c}{c n_g \epsilon_0 \hbar \gamma_P}, \quad (6)$$

is the resonant cross section describing the interaction between carriers and photons in the active region [68]. Φ is the dipole transition matrix element and Γ_y the transverse confinement factor.

$$\Delta^T(\theta) = 2 \frac{\delta^T(\theta, N(\theta)) - \alpha \sigma_D}{\Gamma(N(\theta))} - \alpha, \quad (7)$$

is the effective cavity detuning [47,69]. It depends on N and T through the carrier and temperature-dependent peak-gain shift [70]. However as both δ^T and Γ have similar (functional) dependence on N [71], carrier dependence of Δ^T is known to be weak for quantum confined active media [48] and hence has been omitted from Eq. (7). Also, as explicit temperature dependence of Γ is not considered in this work, Δ^T depends on temperature only through the temperature-induced band-gap shift. This allows us to define carrier-independent but temperature-dependent detunings as follows [43,44]. The net cavity detuning is

$$\delta^T = \theta + \Omega + \vartheta^T, \quad (8)$$

with

$$\theta = \frac{\omega_0^{Hom} - \omega_0^{Inh}}{\gamma_P}, \quad (9)$$

and

$$\Omega = \frac{\omega_0^{Inh} - \omega_c}{\gamma_P} \quad (10)$$

is the conventional peak gain-cavity detuning. ω_0^{Inh} is the center of the inhomogeneous line and ω_0^{Hom} is the resonant frequency of a homogeneous packet (a set of equal sized and shaped QD's) inside the inhomogeneous profile, Fig. 1. δ^T (and hence Δ^T) depends on temperature via temperature-induced band-gap shrinkage [$\omega_0^{Hom} \equiv \omega_0^{Hom}(T)$] [70]. This temperature dependence can be written as an additional detuning $\vartheta^T = \delta \omega_0^{Hom}(T) = \delta E_g(T) / \hbar$ [$\delta E_g(T) < 0$] added to θ as in Eq. (8). Temperature dependence of ω_0^{Hom} is calculated using Varshni's approximation [72]. Ω plays the important role of tuning the laser line above resonance (negative cavity detuning) and below resonance (positive cavity detuning), Fig. 1. It is well known that cavity detuning is responsible for selection of spatial modes in wide-aperture structures. This has been verified both theoretically [73] and experimentally [74,75]. It is helpful at this point to define a new detuning Ω^T for the linear stability analysis to follow as

$$\Omega^T = \Omega + \vartheta^T. \quad (11)$$

$\Lambda(x) = J(x) / (q_e d_{act})$ is the pump parameter and is dependent on the lateral dimension through current spreading. $J(x)$ is the current density calculated self-consistently using a steady-state electrothermal model [76] for the full multilayer laser structure, q_e the electronic charge, and d_{act} the thickness of the QD active layer [77]. γ_N is the effective carrier-recombination rate in the active layer and D the in-plane carrier diffusion coefficient. Carrier dependence of Γ is chosen twice as in QW media [78,79], equal to $\sqrt{N/N_{th}}$ with threshold carrier density $N_{th} = 2N_{tr}$ [71]. We find that the same carrier dependence holds for δ^T too, when fitted to experimental data [41] to a close approximation. This is not surprising as Δ was also found to have a very weak dependence on N for a QW laser [48]. Also, this choice eases both analytical and numerical handling.

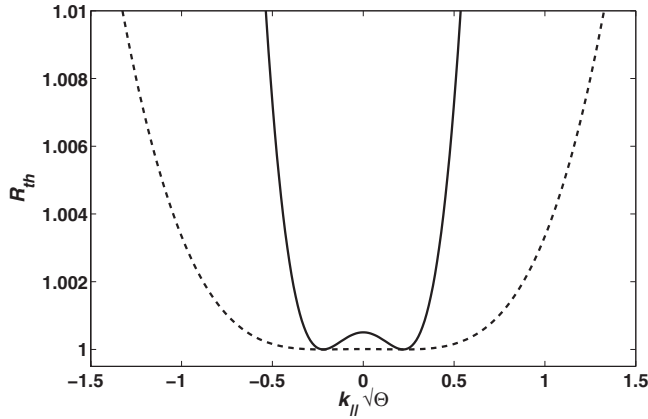


FIG. 2. Neutral stability curve for positive detuning ($\Omega=0.1$). Homogeneous ($\sigma_D=0$, solid line) and inhomogeneous broadening ($\sigma_D=3$, dashed line).

The carrier and temperature dependence of α and a_n is not considered in this work. This is a valid approximation for operating points not too high above threshold [41]. An accurate analysis at higher pump powers would require systematic experimental determination of gain, dispersion, differential gain, alpha-parameter, etc. in quantum-dot lasers which can then be fitted to simple analytical functions and used with the theory developed here. Such an experimental study is only available at present for far-infrared QD lasers [41] and not in the near-infrared region, the primary wavelength region of interest for this paper. As one cannot generalize results of [41] for use in the near-infrared region at all carrier densities above threshold, we keep our analysis restricted to twice threshold in this work. Otherwise our model is valid at all pumping levels.

The polarization equation in the non-two-level form Eq. (2) was originally derived for a homogeneously broadened semiconductor diode laser [48,56]. It has recently been derived by Prati *et al.* [71] using a different and independent approach, again for a homogeneously broadened semiconductor gain medium. We have extended this derivation to the inhomogeneous broadening case by self-consistently incorporating carrier and temperature effects [47]. We also explicitly write the alpha-parameter, gain, and differential gain in Eq. (2), unlike in [48,71]. Conventional homogeneously broadened [i.e., $\sigma_D=0$, $\tilde{g}(\theta)=\delta_{Dirac}(0)$] semiconductor laser rate equations [80] in the nonthermal regime [$\delta_n^T(x)=0$] are recovered from the above set of Maxwell-Bloch equations upon (i) adiabatic elimination of the polarization using Eq. (2) (ii) using the usual approximation that in the vicinity of threshold the lasing frequency is $\omega_L=\omega_c+\kappa_E\alpha$ (mode pulling), and then (iii) projecting the resulting Eqs. (1)–(3) onto ω_L [63]. However, it should be noted that the aforementioned “mode-pulling approximation” is fragile as the lasing frequency is *a priori* unknown and is instead established via a dynamic competition between material and cavity resonances as the laser approaches a steady state. Its usage is suitable only in the vicinity of laser threshold. This suggests that to investigate the true nature of lasing phenomena the full set of Eqs. (1)–(3) should be used instead of simplistic rate equations. The conventional two-level, temperature-

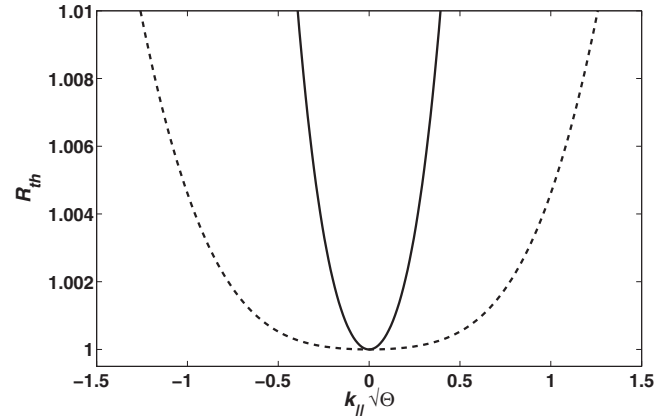


FIG. 3. Neutral stability curve for negative detuning ($\Omega=-0.1$). Homogeneous ($\sigma_D=0$, solid line) and inhomogeneous broadening ($\sigma_D=3$, dashed line).

independent, homogeneously broadened Maxwell-Bloch equations [37] can also be recovered from Eqs. (1)–(3), under the two-level approximation, $\Delta^T=\alpha$ [71] and assuming that Γ is carrier independent. Note that the two-level approximation is farfetched for lasers with semiconductor gain media as Δ^T is generally too small to be set equal to α .

The electrothermal model employed for the calculation of lateral current density and temperature profile which go into Eqs. (1)–(3) is fully described in our earlier work [76]. These calculations have been recently verified for 950 nm emitting broad-area QD lasers [81]. Here we describe only the manner in which it is incorporated in our modal analysis. As already mentioned in the introduction, we work in a time window where the material polarization, field, and carriers see a constant temperature as they evolve in time. Hence it is appropriate to model heat and carrier transport in steady state. We solve the heat conduction equation coupled with Laplace’s equation (for current spreading) on a 2D lateral cross section of the laser epitaxial structure [76]. The oxide-insulated edge emitting QD laser diode with a 50 μm planar stripe and a cavity length of 1 mm used in our model has an experimental threshold current of 460 mA in the normal *p*-down bonding configuration. For wide-aperture QD laser diodes, unlike their QW counterparts, inhibited in-plane carrier diffusion is believed to cause reduced facet heating with peak facet temperatures comparable to those in bulk [82]. As the field spends very little time ($< \text{ps}$) near the facets, such small differences in temperature-induced index change at the facets compared to the bulk should have negligible effect on the spatial mode structure. This justifies our mean-field modal analysis and facilitates the use of a 2D electrothermal model instead of 3D.

III. LINEAR STABILITY ANALYSIS

Linear stability analysis is a powerful tool to study the stability of spatial frequencies selected at the onset of laser emission (first laser threshold), especially in wide-aperture lasers [73]. Starting with a small perturbation around the nonlasing solution $E=0$, $P=0$ and $N=\bar{N}$ ($\bar{N}=\bar{\Lambda}+N_r$, and $\bar{\Lambda}$

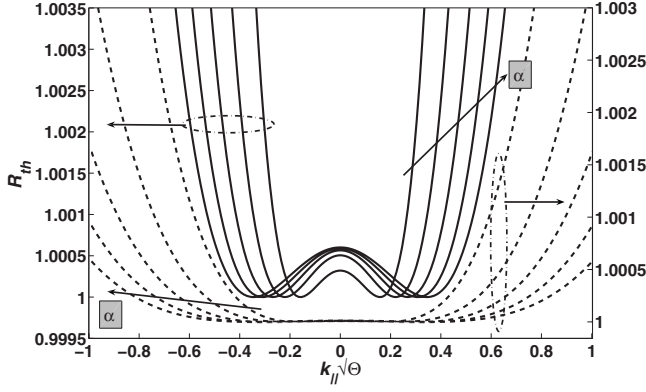


FIG. 4. Neutral stability curves for positive detuning ($\Omega=0.1$) for increasing values of α (1–5). Homogeneous ($\sigma_D=0$, solid lines) and inhomogeneous broadening ($\sigma_D=3$, dashed lines).

$=\Lambda\gamma_N^{-1}-N_{tr}$), expanding the variables in the spatial frequency $k_{||}$ space as

$$\begin{pmatrix} E \\ P \\ N \end{pmatrix} = \begin{pmatrix} 0 \\ 0 \\ \bar{N} \end{pmatrix} + \begin{pmatrix} \delta E_{k_{||}} \\ \delta P_{k_{||}} \\ \delta N_{k_{||}} \end{pmatrix} e^{ik_{||}x + \xi t}, \quad (12)$$

and substituting them in Eqs. (1)–(3) one obtains a system of equations for each set of Fourier components ($\delta E_{k_{||}}$, $\delta P_{k_{||}}$, and $\delta N_{k_{||}}$) [46]. The carrier Eq. (3) as usual does not contribute to any instabilities [46,73] whereas field and polarization Eqs. (1) and (3) lead to an equation for the eigenvalues ξ [46]. The real part of ξ [$\text{Re}(\xi)=\xi_{\text{Re}}$] describes the growth ($\xi_{\text{Re}} > 0$) or decay ($\xi_{\text{Re}} < 0$) of spatial-mode instabilities in the vicinity of laser threshold, with $\text{Im}(\xi)=\xi_{\text{Im}}$ giving the corresponding frequency of instability pulsations. As one crosses the first laser threshold, ξ_{Re} changes sign from negative to positive [46]. Thus we look for the neutral-stability condition $\xi_{\text{Re}}=0$, which describes the first laser threshold, the onset of cw lasing [83]. For the inhomogeneously broadened quasi-two-level Maxwell-Bloch equations outlined above, closed form analytical expressions from linear stability analysis are possible only for a Lorentzian gain profile [46]

$$\tilde{g}_L(\theta) = \frac{\sigma_D}{\pi} \frac{1}{\theta^2 + \sigma_D^2}, \quad (13)$$

instead of the Gaussian Eq. (4). Analysis with a Gaussian profile requires numerical techniques but leads to qualitatively similar results [46] and is therefore not described here. But as we will see below, our expressions obtained for the inhomogeneous broadening case reduce to well-known equations for the homogeneous broadening case validating the above approximation. The eigenvalue equation for $\tilde{\xi}^{\text{inh}}$ $=\xi^{\text{inh}}/\gamma_P$ ($\xi=\xi^{\text{inh}}$, for inhomogeneous broadening case) with rescaled variables $\Theta=A/\gamma_P$ and $\sigma_E=\kappa_E/\gamma_P$ is

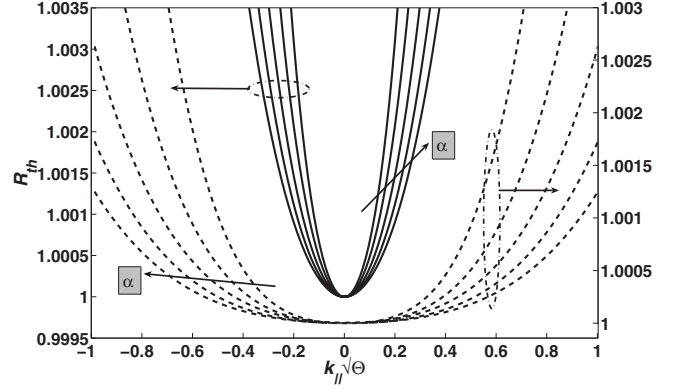


FIG. 5. Neutral stability curves for negative detuning ($\Omega=-0.1$) for increasing values of α (1–5). The curves overlay on each other for each broadening type.

$$\begin{aligned} &\sigma_E + i[\tilde{\xi}^{\text{inh}} + \Theta k_{||}^2 - \sigma_E \delta_n^T] \\ &= R_{th}^{\text{inh}}(1 - i\alpha) \left[\frac{(1 + 2\sigma_D)(1 - i\alpha) + 2i\Omega^T}{(1 + 2\sigma_D)(1 - i\alpha) + 2i\Omega^T + i\tilde{\xi}^{\text{inh}}} \right], \end{aligned} \quad (14)$$

for the general case of temperature-dependent cavity detuning. Separating the above equation into real and imaginary part, one can extract the rescaled laser threshold $R_{th}^{\text{inh}} = a_n \tilde{\Lambda}/(2\gamma_P)$ and the rescaled pulsation frequency $\tilde{\xi}_{\text{Im}}^{\text{inh}}$ of the first Fourier mode to appear at the onset of lasing. Discarding the negative threshold obtained from the above eigenvalue equation Eq. (14) (a quadratic in $\tilde{\xi}^{\text{inh}}$), the neutral stability curves [R_{th}^{inh} vs $k_{||}\sqrt{\Theta}$ (rescaled spatial frequency)] are plotted in Figs. 2–7 for different cases discussed below. Simple analytical expressions for R_{th}^{inh} and $\tilde{\xi}_{\text{Im}}^{\text{inh}}$ cannot be derived directly from Eq. (14). However, in the two-level approximation (TLA) mentioned above, simple analytical results are possible where the expression for R_{th}^{inh} and $\tilde{\xi}^{\text{inh}}$ reduce to a more familiar form [46]

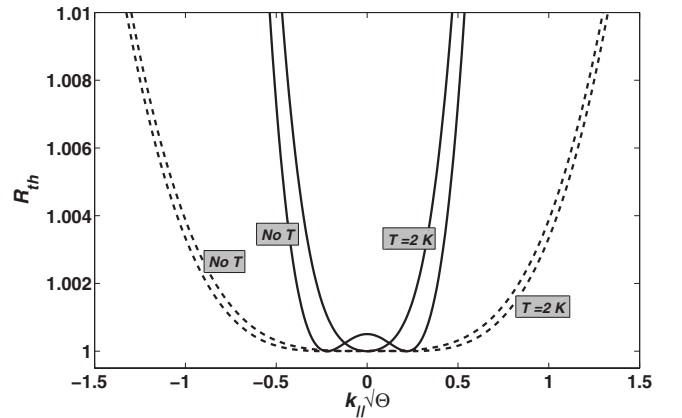


FIG. 6. Neutral stability curves for positive detuning ($\Omega=0.1$) with and without the effect of temperature. Homogeneous ($\sigma_D=0$, solid lines) and inhomogeneous broadening ($\sigma_D=3$, dashed lines).

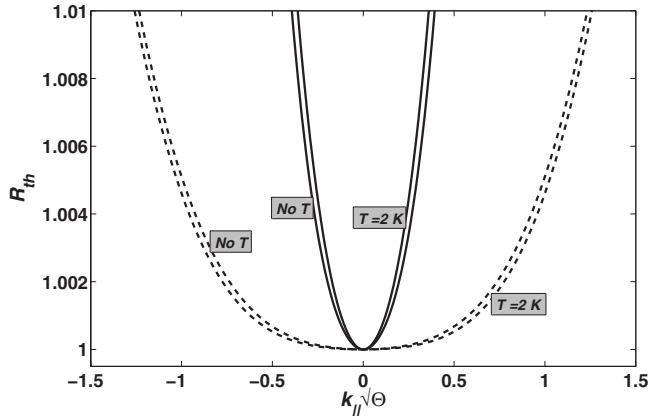


FIG. 7. Neutral stability curves for negative detuning ($\Omega = -0.1$) with and without the effect of temperature. Homogeneous ($\sigma_D = 0$, solid lines) and inhomogeneous gain medium broadening ($\sigma_D = 3$, dashed lines). $k_{||} = 0$ is selected for both types of broadening.

$$R_{th}^{inh,TLA} = \frac{\sigma_E^2}{1 + \alpha^2} \left[1 + \left(\frac{(1 + 2\sigma_D)\alpha + \sigma_E \delta_n^T - k_{||}^2 \Theta}{1 + \sigma_E + 2\sigma_D} \right)^2 \right], \quad (15)$$

and

$$\tilde{\xi}_{lm}^{inh,TLA} = -(1 + 2\sigma_D) \left[\frac{\alpha \sigma_E + k_{||}^2 \Theta - \sigma_E \delta_n^T}{1 + \sigma_E + 2\sigma_D} \right], \quad (16)$$

with α now taking the role of effective cavity detuning. Except for the scaling factor of $\sigma_E^2 [1 + \alpha^2]^{-1}$ in expression (15), one finds that both Eqs. (15) and (16) have a similar form as for conventional two-level inhomogeneously broadened [46] and homogeneously broadened ($\sigma_D = 0$) Maxwell-Bloch equations [73] in the nonthermal regime ($\delta_n^T = 0$). We stress again that considering α equivalent to cavity detuning is improper for semiconductor lasers as we have already mentioned before and Eqs. (15) and (16) are thus only approximate results. Nevertheless the above Eq. (15) gives us important clues toward spatial frequency selection in an inhomogeneously broadened semiconductor lasers at lasing threshold. Two important points are worth noting in the expression for $R_{th}^{inh,TLA}$. First, we see that with an increase in the degree of inhomogeneous broadening (i.e., for larger σ_D) in the gain medium, the lasing threshold becomes independent of the term that selects the spatial frequencies in the nonthermal ($\delta_n^T = 0$) regime. This is validated in our numerical simulation results below with the full set of (non two-level) Maxwell-Bloch Eqs. (1)–(3), for an inhomogeneously broadened gain medium ($\sigma_D = 1.5$ and 3) in the nonthermal regime. However, in the thermal regime, the detuning $\sigma_E \delta_n^T$ due to temperature, which is always positive and greater than gain-cavity detuning forces the laser to emit off-axis (i.e., a double lobed far-field) as elucidated below in our numerical simulations.

A. Nonthermal regime [$\delta_n^T(x) = 0$, $\Omega^T = \Omega$]

We first present results in the nonthermal regime [$T(x) = 0$]. Below we show the neutral stability curves for both

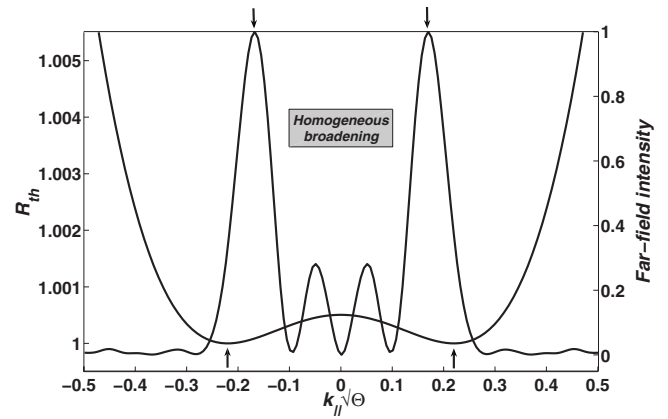


FIG. 8. Neutral stability curve for positive detuning ($\Omega = 0.1$) and for homogeneously broadened ($\sigma_D = 0$) gain medium. There is a close match between numerically calculated far-field profile at threshold and linear stability analysis. Note that the dominant far-field lobe peaks are close to $k_{||} = \pm \sqrt{\Omega/\Theta}$ which has minimum threshold.

positive and negative detuning Ω and for both homogeneous and inhomogeneous broadening case. All neutral stability curves are normalized with respect to their respective minimum threshold values as is customary in literature [46]. The cavity detuning Ω is chosen as ± 0.1 unless otherwise specified and we choose $\alpha = 2$. This cavity detuning is much more than the adjacent spatial mode spacing (in frequency) for the chosen stripe width, allowing existence multiple spatial modes between the fundamental mode and the gain peak. Figure 2 indicates that for positive detuning homogeneously broadened media support two stable spatial frequencies, symmetric about zero, having minimum lasing threshold. The spatial frequencies are close to $k_{||} = \pm \sqrt{\Omega/\Theta}$, similar to a homogeneously broadened two-level medium [73]. This is the well-known off-axis emission [84]. For negative detuning, emission is on-axis with $k_{||} = 0$, which has the minimum lasing threshold, compare Figs. 2 and 3. The reason why positive cavity detuning leads to off-axis emission (dual-lobed far-field, Fig. 8) in a homogeneously broadened medium is directly related to the fact that higher-order spatial modes (corresponding to the positively detuned longitudinal mode) have higher optical frequencies and hence are closer to the gain peak. Therefore a spatial mode with $k_{||} \neq 0$ experiences higher gain and reaches threshold first. On the other hand for negative detuning the fundamental spatial mode ($k_{||} = 0$) is closest to the gain peak and attains threshold first. Inhomogeneously broadened gain media behave differently as they have the ability to saturate inhomogeneously enabling the spatial modes to extract gain locally. Therefore for an inhomogeneously broadened medium the selection of $k_{||}$ at threshold is less restrictive and the neutral stability curve shows a general flattening around the minima for both positive and negative detunings; see Figs. 2 and 3 [46]. The flattening of the neural stability curve for inhomogeneous broadening in our case is similar to the one reported by Cabrera *et al.* [46], with the flattening increasing with the degree of inhomogeneous broadening. This indicates that there is a strong competition between the different spatial frequen-

cies close to the fundamental, all of which have extremely close thresholds. Indeed, two symmetrically placed local minima around $k_{\parallel}=0$ can be resolved in the neutral stability curve as in [46], for the inhomogeneous broadening case under positive cavity detuning, however, numerical simulation shows that $k_{\parallel}=0$ state is always selected at and above threshold indicating the fundamental spatial frequency wins the competition in the inhomogeneous broadened medium, irrespective of the order of spatial mode in the near field. It should be kept in mind that linear stability analysis is somewhat idealistic as it assumes an infinite pump profile and hence a continuous set of k_{\parallel} . A real laser has a finite pump profile and hence k_{\parallel} forms a discrete set. It should also be noted that a lower order spatial mode can result in a single lobed far field but will not be diffraction limited unlike a fundamental mode with $k_{\parallel}=0$.

We have used linear stability analysis to check the effect of α on the selection of spatial frequencies at lasing threshold. It is apparent that for a homogeneously broadened medium and for a fixed positive detuning, increasing α selects spatial frequencies which are further apart, Fig. 4. On the contrary α has no effect on spatial frequency selection for a positively detuned inhomogeneously broadened medium, Fig. 4. For negative gain-peak cavity detuning, again spatial frequency selection is independent of α , and the fundamental spatial frequency is always selected at threshold for both broadening types; see Fig. 5. Note that as we are changing α , the mode-pulling approximation mentioned earlier comes into play [71]. This is a promising feature for high brightness wide-aperture QD lasers. This indicates that α (>0) does not act like cavity detuning as is generally assumed [37,52,53], but is related to the coupling of dispersion with gain saturation.

B. Thermal regime [$\delta_n^T(x) \neq 0$]

In the thermal regime two competing effects influence the gain-cavity detuning: shift of the transition frequency for each homogeneous packet via temperature-induced band-gap shrinkage [85] which leads to the cavity being slightly negatively detuned and the effect of temperature-induced background refractive index perturbation which adds to the cavity detuning [see Eq. (15)]. Band-gap-induced negative detuning is generally thought to counter the antiguiding effect due to carrier induced refractive index change [37]. However, such an assumption is erroneous as this detuning contribution can be shown to be an order of magnitude smaller [~ -0.1 at threshold, $\delta T(x)=1.5$ K] than α . At threshold, band-gap-induced negative detuning is just barely able to overcome the combined positive detuning due to junction temperature-induced index change and gain-cavity detuning Ω . Hence the neutral stability curves for both homogeneous and inhomogeneous broadening flatten near $k_{\parallel}=0$, for positive Ω (Fig. 6). However, as we will see in the numerical simulation results, at pumping levels above threshold, positive detuning due to junction temperature-induced index change is much stronger and band-gap shrinkage is unable to compensate for it. For $\Omega < 0$, both homogeneous and inhomogeneously broadened media behave analogous to the nonthermal case,

selecting $k_{\parallel}=0$, Fig. 7. But again as numerical simulations show, the $\Omega < 0$ case behaves similarly to the $\Omega > 0$ case above threshold.

It can be checked easily, by adiabatic elimination of the polarization Eq. (2), that temperature-induced index change negates the antiguiding contribution from α . But at the same time, it is worth noting that although temperature-induced refractive index change produces a positive guiding mechanism for the propagating field in real space, it cannot prevent the higher-order modes to lase, as in the optical frequency space its effect is to increase the positive detuning, which provides the necessary gain for a higher-order mode with $k_{\parallel} \neq 0$. Thus the net effect of junction temperature rise is to increase the far-field interlobe distance as pumping increases for both positive and negative gain-cavity detuning. This is known from experiments [1,86,87], sophisticated theoretical treatments, and numerical simulations [38,39]. However no clear explanation has been given so far. The result of our linear stability analysis provides the answer in terms of an additional temperature-induced detuning contribution to Ω . This is further validated in our numerical simulations.

Although linear stability analysis is necessarily based upon simplistic approximations, its agreement with the full numerical simulation is excellent (see Fig. 8). The far field at threshold for the positively detuned homogeneous broadening case matches closely to that predicted by linear stability analysis Fig. 8. As we will see in the next section from results of numerical simulations, the threshold behavior predicted by linear stability analysis also matches very closely to numerical solution of full system (1) and (2), for all cases.

IV. NUMERICAL SIMULATIONS: ANALYSIS BEYOND THRESHOLD

A complete study of the Maxwell-Bloch Eqs. (1)–(3) beyond laser threshold requires numerical techniques. The numerical approach, however, is made difficult by the integral over material polarization in Eq. (2), which renders system (1)–(3) infinite dimensional. There is no straightforward way to solve such a system. Two approaches have been suggested in the literature, one due to Graham and Cho [88] and the other by Idiatulin and Uspenskii [89]. Graham and Cho defined macroscopic variables for the total polarization and inversion and reduced the infinite-dimensional system to a set of four equations, allowing analytical tractability. However, this approach requires an infinite hierarchy of coupled equations generated in the reduction procedure to be truncated by a judicious choice of some adjustable parameters while introducing idealistic approximations [46,88]. Moreover, its equivalence to the infinite-dimensional system is valid only in the stable regime of solutions [90] making it unsuitable for investigating unstable filamentary modal behavior. We use the Idiatulin and Uspenskii approach instead, which relies on suitably discretizing Gaussian (4) in the spectral domain yielding a finite-dimensional system of equations [36,46,90]. It has already been shown that using two suitably spaced spectral components about the Gaussian line center can lead to a system equivalent to the infinite-dimensional system in both the steady-state and chaotic regime [46,90]. Introduc-

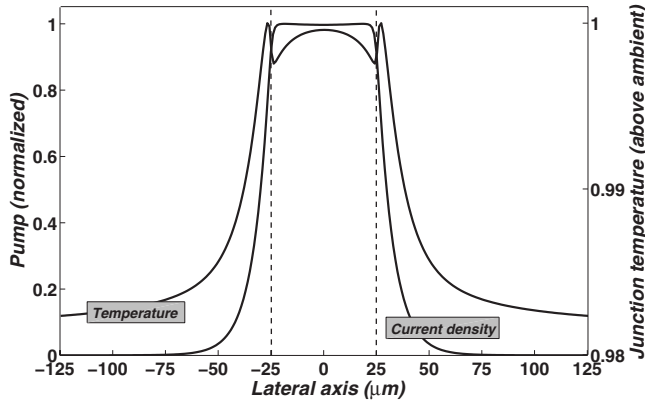


FIG. 9. Lateral junction pump and temperature profiles (normalized) calculated from the self-consistent electrothermal model [76]. The active stripe is indicated by dashed lines

tion of two more spectral components including the central (total five) makes the reduced finite-dimensional system robust enough to handle spatial instabilities [46]. Choosing symmetrically placed spectral components reduces the infinite-dimensional system into a system where only positive values of detuning θ need to be considered. A proper choice of spectral components is critical in describing the spatiotemporal behavior of the system. We choose the spectral components such that [36,90,91].

$$\int_0^\theta \tilde{g}(\theta)d\theta = \int_\theta^\infty \tilde{g}(\theta)d\theta. \quad (17)$$

All equations discussed above, including heat and Laplace's equation have been solved using the finite element method under the Galerkin approximation [92]. For solving system (1)–(3), we use absorptive boundary conditions at the lateral boundaries of the computational window [23,24] and an adaptive discretization in both space (maximum resolution 1 μm) and time (maximum resolution 1 fs). This prevents introduction of spurious numerical artifacts and instabilities in the already unstable physical solutions of the problem at hand. For a 50 μm wide stripe we choose a 512 μm wide lateral computational window. Unlike the Maxwell-Bloch model, where we use adaptive mesh refinement, the steady-state electrothermal model uses a fixed hexahedral mesh [76].

Figure 9 shows the pump and junction temperature profiles calculated from our steady-state electrothermal model [76], using full epitaxial structural details of the QD device [77]. Similar to a broad area QW laser [76], the QD laser also shows a kink in the junction temperature profile just outside the stripe and a bulge inside the stripe. Note also that the pump profile is relatively smooth at the stripe edges unlike the temperature profile. Previously, all models have assumed a top-hat pump profile with sharp corners (hence index steps) at the stripe edges [26]. Such index steps have been speculated to cause lateral field instabilities [26]. However, as seen from Fig. 9, the thermal index steps at the stripe edges are more likely to reflect the lateral traveling waves [58].

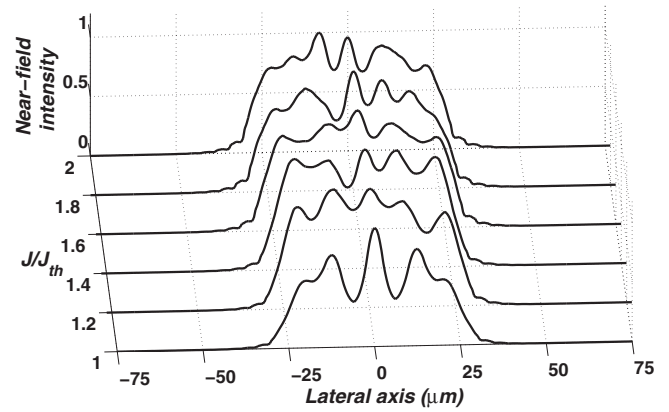


FIG. 10. Nonthermal regime: near field for positively detuned ($\Omega=0.1$) homogeneously broadened ($\sigma_D=0$) gain medium at different pump levels. Profiles for negative detuning are qualitatively similar. Filamentary modal structure is evident.

The near- and far-field profiles shown below are time averaged. We found significant qualitative differences between time averaged profiles for 5 ns to 10 ns runs for both thermal and nonthermal regime. But for time averaged profiles with 15 ns and/or 50 ns runs there was no qualitative difference. We therefore chose 20 ns runs for this work. Values of the parameters used in numerical calculation are as follows: $\kappa_E = (2\tau_P)^{-1}$, $\tau_P=4$ ps (photon decay time) [71], $\gamma_P=10^{13}$ Hz [52], $\gamma_N=\tau_N^{-1}$, $\tau_N=1$ ns [15], $D=3$ $\text{cm}^2 \text{s}^{-1}$ [61], $\beta_T=4 \times 10^{-4}$ [85], $\omega_c=2\pi c\lambda_c^{-1}$, $\lambda_c=0.8$ μm , $n_e=3.3$, $n_g=4.2$, $N_{tr}=10^{18}$ cm^{-3} , and $\alpha=2$.

A. Nonthermal regime [$\delta_n^T(x)=0$]

Figure 10 shows the near-field intensity profiles at different pump levels above threshold, for $\Omega > 0$ and homogeneous broadening. For $\Omega < 0$, the profiles are qualitatively the same. Note that the sign of cavity detuning directly affects the spatial phase of the modes as well as their spectral position relative to the gain peak. Thus, at first glance it would appear that the spatial mode intensity structure should also be strongly dependent on the sign of cavity detuning like the corresponding spatial frequency spectra, as indicated by our linear stability analysis above and the numerical simulation below, for a homogeneously broadened gain medium. However, higher-order spatial modes have higher diffraction losses and extract most of their gain spatially and very less spectrally, making the near-field intensity profiles qualitatively similar for both signs of cavity detuning. We find that the mode order in the near field is independent of Ω , even at threshold. Note that increasing the pump selects higher-order spatial modes as expected, Fig. 10. This feature is captured in our model as it includes a proper description of the change in gain and dispersion vs carrier density in the gain medium. Two important differences are apparent between the near-field structure in the homogeneously broadened medium in comparison to the inhomogeneously broadened medium; see Fig. 11. First, the near field in the homogeneously broadened medium shows stronger filamentary behavior than the inhomogeneous case, and second the

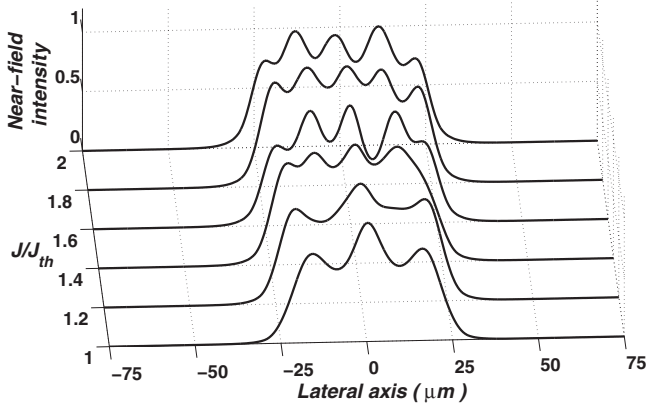


FIG. 11. Nonthermal regime: near field for positively detuned ($\Omega=0.1$) inhomogeneously broadened ($\sigma_D=3$) gain medium at different pump levels. Profiles for negative detuning are qualitatively similar. Note the reduced filamentation compared to homogeneous case.

inhomogeneously broadened medium sustains lower order spatial modes in comparison to the homogeneously broadened medium at similar pump levels. The latter effect can be attributed to inhomogeneous gain saturation in the inhomogeneously broadened quantum-dot gain medium.

Pump-dependent far-field profiles are shown in Figs. 12–14. Figure 12 shows the homogeneous case, where at threshold, positive detuning selects two spatial wave numbers symmetrically placed about zero as predicted by linear stability analysis. For negative detuning, threshold behavior is same as predicted by linear stability analysis where $k_{||}=0$ is selected. This indicates that the contribution of the fundamental mode is much stronger for $\Omega < 0$ than for $\Omega > 0$, as the corresponding near-field intensity profiles have the same mode order, independent of the sign of Ω . Above threshold the far field shows random single and double-lobe behavior as a function of pump. Figure 14 shows the inhomogeneous case for both positive and negative detuning with moderate inhomogeneous broadening $\sigma_D=1.5$. The pump-dependent far field already shows more single lobe states than double-lobe states for both signs of detuning. Note that higher

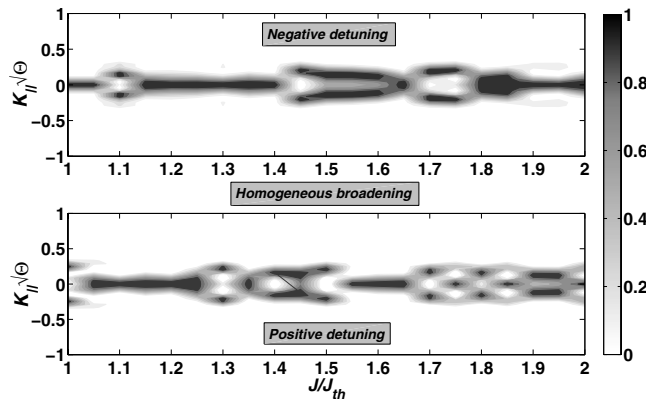


FIG. 12. Nonthermal regime: far-field profiles in a homogeneously broadened ($\sigma_D=0$) gain media for both signs of detuning ($\Omega = \pm 0.1$) at different pump levels. The far-field profile moves between single and double lobes.

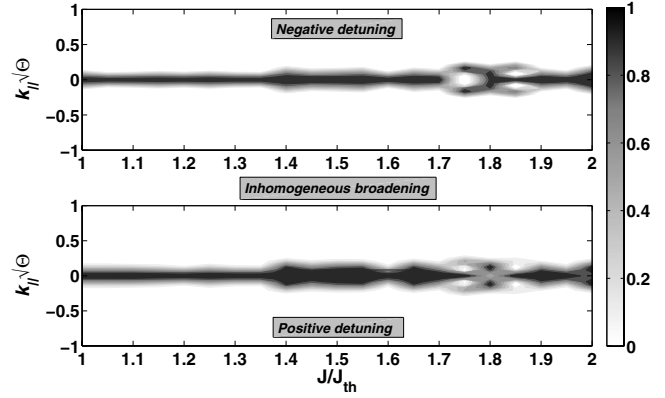


FIG. 13. Nonthermal regime: pump-dependent far field in moderately inhomogeneously broadened ($\sigma_D=1.5$) gain medium for both signs of detuning ($\Omega = \pm 0.1$). Difference between negatively detuned homogeneously broadened medium is already evident.

pumping results in broader single lobes or double lobes in the far field, indicating stronger contribution from higher-order spatial modes. With a further increase in the strength of inhomogeneous broadening ($\sigma_D=3$), both signs of detuning show a single-lobe state until twice threshold (see Fig. 14), independent of the higher-order modes appearing in the near field, Fig. 11. This is in striking contrast to the homogeneous case and occurs because the selection of spatial frequencies becomes independent of pump and detuning with increasing strength of inhomogeneous broadening, as already mentioned in the previous section. Note, however, that the width of the single lobe gradually broadens as pumping increases. One might speculate that at much higher operating points the single lobe is likely to break into a double lobe. However such an analysis is beyond the scope of this work. Nevertheless, the finding that an inhomogeneously broadened medium selects on-axis emission above threshold in the nonthermal (quasi-cw) regime independent of gain-cavity detuning is of immense importance and may prove significant in designing future wide-aperture QD lasers with improved beam quality.

We have found exactly the same behavior with further increase in the degree inhomogeneous broadening, where

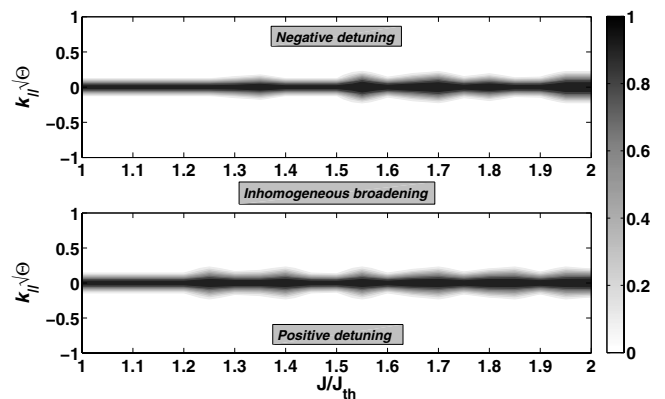


FIG. 14. Nonthermal regime: far field at different pump levels in an inhomogeneously broadened ($\sigma_D=3$) gain media for both signs of detuning ($\Omega = \pm 0.1$). The far field remains single lobed until twice threshold.

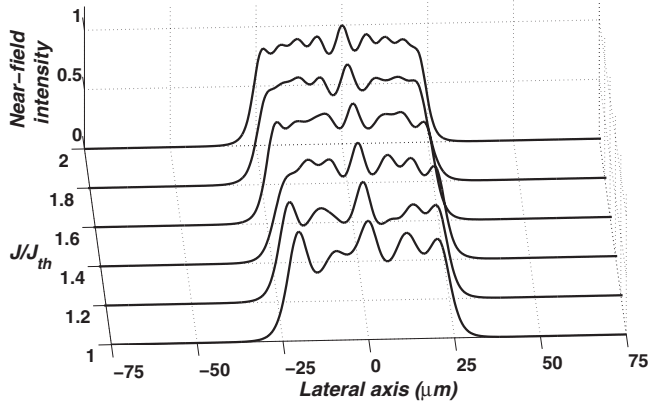


FIG. 15. Thermal regime: pump resolved near field for positively detuned ($\Omega=0.1$) homogeneously broadened ($\sigma_D=0$) gain medium. Profiles for negative detuning are qualitatively similar.

emission remains on-axis up to $\sigma_D=5$, beyond which we did not run numerical simulations. However, a direct comparison of $\sigma_D=5$ with a homogeneously broadened medium is not appropriate, as it is known from two-level models, that an inhomogeneously broadened gain medium exhibits an increased lasing threshold in comparison to a homogeneous gain medium [46]. This happens because the external pump pumps all homogeneous packets under the inhomogeneous line shape equally, whereas the gain is utilized only in vicinity of the cavity resonance and the rest remains unused unlike in a homogeneous medium where gain saturates homogeneously. Thus, part of the pump remains unused and the threshold is higher for an inhomogeneously broadened medium in comparison to the homogeneous case. We find that for $\sigma_D=3$, the numerically calculated lasing threshold to be 2.1 times higher than that for $\sigma_D=0$ (homogeneous case). Nevertheless, as a lower order spatial mode is selected at the onset of lasing in the inhomogeneous medium in comparison to the homogeneous medium; see Figs. 10 and 11, even for a higher lasing threshold, an increased threshold should not hinder a comparison for $\sigma_D=3$.

B. Thermal regime [$\delta_n^T(x) \neq 0$]

Figures 15 and 16 show pump-dependent near-field profiles for positively detuned homogeneous and inhomogeneously broadened gain media. Similar to the nonthermal regime, the negative detuning case shows qualitatively similar profiles. As expected from linear stability analysis, presence of the temperature profile has a twofold effect on the near-field structure. First, beyond threshold the order of mode excited is higher in comparison to the nonthermal regime as predicted by linear stability analysis, due to additional thermal detuning. At threshold, however, a lower order mode is selected in the inhomogeneously broadened medium in comparison to the homogeneous case, aided by the reduction in thermal detuning via temperature-induced band-gap decrease. Second, as filament size is inversely proportional to the square root of index step [94] the filaments are smaller due to temperature-induced refractive index increase in the homogeneously broadened medium. Again, the near-field

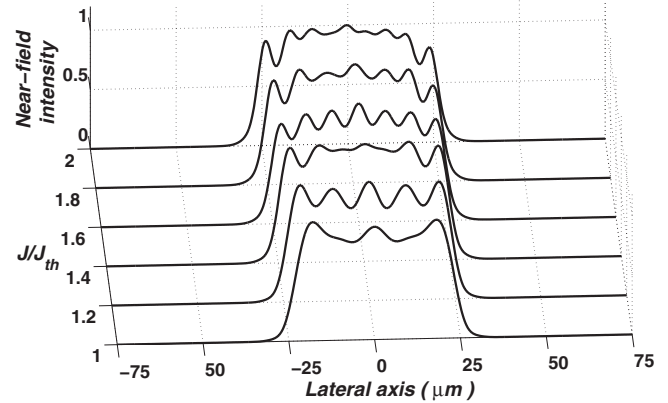


FIG. 16. Thermal regime: pump-dependent near field for positively detuned ($\Omega=0.1$) inhomogeneously broadened ($\sigma_D=3$) gain medium. Profiles for negative detuning are qualitatively similar. Note that the modal structure is stable, symmetric, and relatively devoid of filamentation. The near-field profiles are simple linear combinations of Hermite-Gaussian functions [93].

profile in the inhomogeneously broadened medium is much cleaner, symmetric, and shows no filamentary behavior. Note that the nonfilamentary near-field profiles in Fig. 16 are linear combinations of Hermite-Gaussian functions [93].

The threshold behavior shown by pump-dependent far fields, see Fig. 17 and Fig. 18, are in agreement with the linear stability analysis for both homogeneous and inhomogeneous broadening and for both positive and negative detuning. Both media support on-axis emission at threshold aided by the negative detuning due to temperature-induced band-gap reduction. In a homogeneously broadened media, as expected from linear stability analysis the interlobe distance increases with pumping above threshold; see Fig. 17. For $\Omega > 0$ the double lobed far field expands into multilobed profiles near twice threshold, Fig. 17. Such multilobed behavior is commonly observed in experiments [1,86,87]. In the thermal regime, inhomogeneous medium behaves analogous to the homogeneous medium, Fig. 18, and the advantage of the inhomogeneous medium in selecting on-axis emission is partly reduced above threshold. However, the spatial frequency spectra are much clearer and stable in the

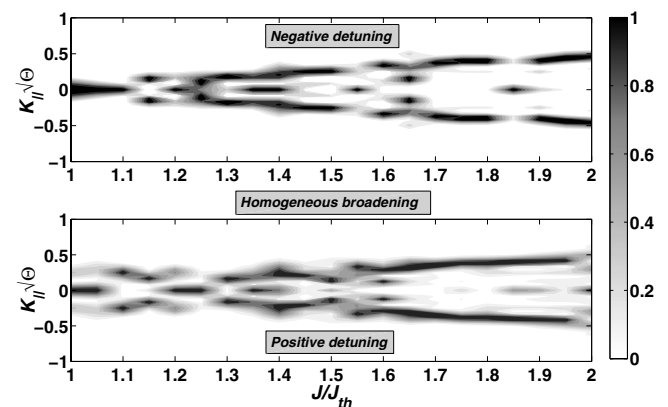


FIG. 17. Thermal regime: pump resolved far field in a homogeneously broadened ($\sigma_D=0$) gain medium for both positive and negative detuning ($\Omega = \pm 0.1$). Far-field broadening is apparent.

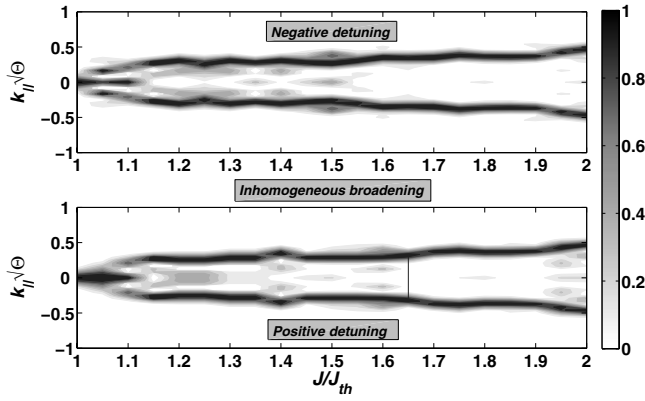


FIG. 18. Thermal regime: Pump dependent far-field in an inhomogeneously broadened ($\sigma_D=3$) gain medium for both positive and negative detuning ($\Omega = \pm 0.1$). Far-field broadening is apparent.

inhomogeneously broadened case. It is worth noting that the mode width of the near field increases with pumping for both types of gain broadening. This is also known experimentally [93] and occurs because higher-order modes, being at higher spatial frequencies, diffract more. Also as mentioned above, it is interesting to note that near-field profiles are qualitatively similar and independent of the sign of cavity detuning in both thermal and nonthermal regimes and for both homogeneously and inhomogeneously broadened gain medium. This is expected as the sign of cavity detuning affects only the spatial phase of the modes and not the intensity.

Finally, we compare above-threshold time-resolved near-field profiles for both broadening types with $\Omega > 0$ and in both thermal and nonthermal regimes. Figures 19 and 20 show the complex spatiotemporal near-field profiles from 6.5 ns after laser switch on until 8.5 ns at 1.5 times threshold. The time slot is arbitrarily chosen, but helps us in comparing with available experimental results [23,87,95]. Unlike the pump-dependent far-field plots where the dark regions have the highest intensities, the white portions within the stripe have the highest intensities in the time-resolved near-field

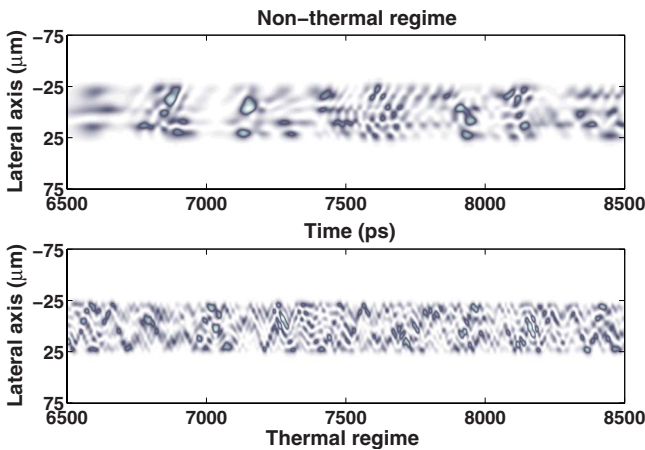


FIG. 19. (Color online) Time-resolved near field (6.5–8.5 ns after laser switch on) for positively detuned ($\Omega=0.1$) homogeneously broadened ($\sigma_D=0$) gain medium for both thermal and non-thermal regimes. The negatively detuned case gives qualitatively similar profiles.

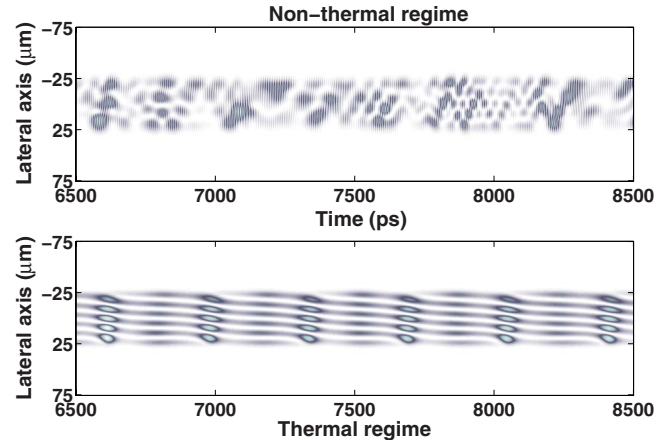


FIG. 20. (Color online) Time-resolved near field (6.5–8.5 ns after laser switch on) for positively detuned ($\Omega=0.1$) inhomogeneously broadened gain medium ($\sigma_D=3$) for both thermal and non-thermal regimes. Negative detuning gives qualitatively similar profiles.

plots. Note the significant difference in dynamics between the thermal and nonthermal regime. In a homogeneously broadened medium in the thermal regime, see Fig. 19, light takes a zigzag path well known from experiments [87,95], going from one edge of the stripe to the other in a periodic fashion. This is more prominent in the thermal regime unlike in the nonthermal regime, where temperature-induced lensing is absent. The lateral waves (with $k_{\parallel} \neq 0$) [58] reflect at the index step created by temperature at the stripe edges and travel from one side to the other. Such behavior has also been seen in experiments with broad area QW lasers, where a period of 100 ps [87] was observed. This periodicity matches very closely with our result for the homogeneously broadened laser in the thermal regime; see Fig. 19. In the nonthermal regime, the only guiding mechanism for the field is through spatially burnt holes (local index guides) in the carrier profile. As spatial hole burning is dynamic in nature, the filaments travel randomly, some of them taking a straighter non-zigzag path. Such behavior is observed experimentally in the quasi-cw regime [95] and again our numerical simulation offers a close match.

The inhomogeneously broadened medium in the nonthermal regime shows self-pulsing in the near-field intensity, a behavior typical of such media, Fig. 20. Although the character of near-field filamentation in the nonthermal regime is not very different from that in homogeneously broadened media, see Fig. 19, we have seen above that the spatial mode spectra (far field) shows marked differences which we attribute to inhomogeneous gain saturation. Surprisingly, the self-pulsing behavior vanishes in the presence of the temperature profile. The reason behind this effect is not yet clear and will be studied further.

A more apparent effect of the temperature profile in the time-resolved near field is the reduction of filament size, as mentioned earlier. Also the zigzag nature of dynamical beam steering seen in the homogeneous medium (thermal regime) is not present in the inhomogeneous medium, where the dynamics occurs on a different time scale. Thus, both qualitatively and quantitatively, inhomogeneous gain media pro-

duce different spatial mode dynamics, not known previously for a semiconductor laser. Although not shown explicitly above, the carrier density is always anticorrelated with the field on a time-averaged basis. On a time-resolved basis, however, there is no definite anticorrelation on account of the different time scales in which field and carrier dynamics take place. We also point out the effect of in-plane carrier diffusion on the spatial mode structure and dynamics: observable differences were found only for very (20 times) high values of the carrier diffusion coefficient. This is expected, as linear stability analysis shows no instability due to carrier diffusion.

V. SUMMARY

In summary, we have theoretically analyzed wide-aperture quantum-dot lasers within the framework of inhomogeneously broadened semiconductor Maxwell-Bloch equations, with particular emphasis on gain broadening and thermal effects. The systematic analysis self-consistently included optical, electrical, and thermal effects with appropriate description of gain and dispersion in the quantum-dot semiconductor active region. Using linear stability analysis, behavior of spatial frequency selection at laser threshold is calculated and high resolution adaptive-grid finite element technique is used to simulate the spatial mode dynamics and spectra above threshold. It is shown via linear stability analysis that in an inhomogeneously broadened gain medium, such as in a QD laser, the neutral stability curve shows a general flattening around $k_{\parallel}=0$, when the cavity is tuned below resonance ($\Omega > 0$), indicating possible selection of a spectrum of spatial frequencies around it. However, numerical simulations show that the fundamental spatial frequency $k_{\parallel}=0$ is always selected at threshold, in both the nonthermal and thermal regimes. For a cavity tuned above resonance ($\Omega < 0$), both linear stability analysis and numerical simulation show that the fundamental spatial frequency $k_{\parallel}=0$ is always selected at threshold in both the thermal and nonthermal regimes. This is unlike a homogeneously broadened gain

medium (a QW laser), where spatial frequency selection at threshold is cavity detuning and temperature dependent. Also, spatial frequency selection at threshold in an inhomogeneously broadened media is independent of phase-amplitude coupling and cavity detuning unlike a homogeneously broadened media where spatial frequency selection depends on phase-amplitude coupling for positive peak gain-cavity detuning. We elucidate through numerical modeling that the presence of inhomogeneous broadening is favorable for on-axis emission in the absence of thermal effects and results in stable single lobed far fields above threshold. This advantage is partly lost in the above threshold thermal-regime due to temperature-induced index increase. However, in the thermal regime the near-field (spatial mode) structure is clearly much more stable in the inhomogeneously broadened medium in comparison to the homogeneously broadened medium implying improved stability of the far field. Time-resolved near fields show very different dynamics in both space and time for homogeneously and inhomogeneously broadened gain media. The difference is especially evident in the thermal regime, where the character of spatial mode dynamics in the two media changes drastically illuminating the effect of gain broadening in spatial mode dynamics. Our concerted theoretical analysis sheds light on spatial frequency selection and spatial mode structure in wide-aperture semiconductor lasers and elucidates the influence of gain broadening and phase-amplitude coupling on it. The Maxwell-Bloch equations developed here can be easily adapted to include longitudinal degree of freedom (multiple longitudinal modes) and will prove useful to study any generic semiconductor laser or amplifier.

ACKNOWLEDGMENTS

This work was supported by Science Foundation Ireland under Grant No. 04/BR/P0701. The authors acknowledge helpful discussions with Dr. Guillaume Huyet, Professor J. V. Moloney, and Professor F. Prati during the course of this work.

-
- [1] M. Behringer, *High Power Diode Lasers. Technology and Applications*, High-Power Diode Laser Technology and Characteristics, edited by F. Bachmann, P. Loosen, and R. Poprawe (Springer, New York, 2007).
 - [2] *High-Power Diode Lasers: Fundamentals, Technology, Applications*, edited by R. Diehl (Springer, New York, 2000).
 - [3] *Semiconductor Lasers II*, edited by E. Kapon (Academic Press, New York, 1998), Chap. 4.
 - [4] N. W. Carlson, *Diode-Laser Arrays* (Springer-Verlag, Berlin, 1994).
 - [5] S. A. Akhmanov, A. P. Sukhorukov, and R. V. Khokhlov, *Sov. Phys. Usp.* **10**, 609 (1968).
 - [6] S. A. Akhmanov, R. V. Khokhlov, and A. P. Sukhorukov, in *Laser Handbook*, edited by F. T. Arecchi and E. O. Schulz-Dubois (North-Holland, Amsterdam, 1972).
 - [7] N. B. Abraham and W. J. Firth, *J. Opt. Soc. Am. B* **7**, 951 (1990).
 - [8] C. S. Liu and V. K. Tripathi, *Interaction of Electromagnetic Waves and Electron Beams with Plasmas* (World Scientific, Singapore, 1994).
 - [9] W. L. Kruer, *The Physics of Laser Plasma Interactions* (Addison-Wesley, Reading, 1988).
 - [10] *Lidar: Range-Resolved Optical Remote Sensing of the Atmosphere*, edited by C. Weikamp (Springer-Verlag, Berlin, 2005).
 - [11] G. H. B. Thompson, *Physics of Semiconductor Laser Devices* (Wiley, New York, 1980).
 - [12] J. C. Dymont, *Appl. Phys. Lett.* **10**, 84 (1967).
 - [13] G. Hunziker and C. Harder, *Appl. Opt.* **34**, 6118 (1995).
 - [14] P. M. Smowton, E. J. Pearce, H. C. Scheider, W. W. Chow, and M. Hopkinson, *Appl. Phys. Lett.* **81**, 3251 (2002).
 - [15] V. M. Ustinov, A. E. Zhukov, A. Y. Egorov, and N. A. Maleev, *Quantum Dot Lasers* (Oxford University Press, New York,

- 2003).
- [16] N. N. Ledentsov, M. Grundmann, F. Heinrichsdorff, D. Bimberg, V. M. Ustinov, A. E. Zhukov, M. V. Maximov, Z. I. Alferov, and J. A. Lott, *IEEE J. Sel. Top. Quantum Electron.* **6**, 439 (2000).
- [17] G. Huyet, D. O'Brien, S. P. Hegarty, J. G. McInerney, A. V. Uskov, D. Bimberg, C. Ribbat, V. M. Ustinov, A. E. Zhukov, S. S. Mikhlin, A. R. Kovsh, J. K. White, K. Hinzer, and A. J. SpringThorpe, *Phys. Status Solidi A* **201**, 345 (2004).
- [18] T. C. Newell, D. J. Bossert, A. Stintz, B. Fuchs, K. J. Malloy, and L. F. Lester, *IEEE Photon. Technol. Lett.* **11**, 1527 (1999).
- [19] S. P. Hegarty, B. Corbett, J. G. McInerney, and G. Huyet, *Electron. Lett.* **41**, 416 (2005).
- [20] H. C. Schneider, W. W. Chow, and S. W. Koch, *Phys. Rev. B* **64**, 115315 (2001).
- [21] P. M. Snowton, E. J. Pearce, H. C. Scheider, W. W. Chow, and M. Hopkinson, *Appl. Phys. Lett.* **81**, 3251 (2002).
- [22] A. V. Uskov, E. P. O'Reilly, D. McPeake, N. N. Ledentsov, D. Bimberg, and G. Huyet, *Appl. Phys. Lett.* **84**, 272 (2004).
- [23] O. Hess and T. Kuhn, *Prog. Quantum Electron.* **20**, 85 (1996).
- [24] I. Fischer, O. Hess, W. Elsaßer, and E. Gobel, *Europhys. Lett.* **35**, 579 (1996).
- [25] O. Hess, S. W. Koch, and J. V. Moloney, *IEEE J. Quantum Electron.* **31**, 35 (1995).
- [26] C. Sailliot, V. Voignier, and G. Huyet, *Opt. Commun.* **212**, 353 (2002).
- [27] J. P. Hohimer, G. R. Hadley, and A. Owyong, *Appl. Phys. Lett.* **52**, 260 (1988).
- [28] J. R. O'Callaghan, J. Houlihan, V. Voignier, G. H. Wu, E. O'Neill, J. G. McInerney, and G. Huyet, *IEEE J. Quantum Electron.* **40**, 1 (2004).
- [29] J. R. Marciano and G. P. Agrawal, *IEEE J. Quantum Electron.* **32**, 590 (1996).
- [30] G. R. Hadley, J. P. Hohimer, and A. Owyong, *IEEE J. Quantum Electron.* **24**, 2138 (1988).
- [31] R. J. Lang, A. G. Larsson, and J. G. Cody, *IEEE J. Quantum Electron.* **27**, 312 (1991).
- [32] C. Chang-Hasnain, E. Kapon, and R. Bhat, *Appl. Phys. Lett.* **54**, 205 (1989).
- [33] J. V. Moloney, R. A. Indik, J. K. White, P. Ru, S. W. Koch, and W. W. Chow, *Proc. SPIE* **2146**, 410 (1994).
- [34] M. Sargent III, M. O. Scully, and W. E. Lamb, Jr., *Laser Physics* (Addison-Wesley, Reading, 1974).
- [35] W. E. Lamb, Jr., *Phys. Rev.* **134**, A1429 (1964).
- [36] B. Meziane and H. Ladjouze, *Phys. Rev. A* **45**, 3150 (1992).
- [37] J. Martín-Regalado, S. Balle, and N. B. Abraham, *IEEE J. Quantum Electron.* **32**, 257 (1996).
- [38] J. V. Moloney, M. Kolesik, J. Hader, and S. W. Koch, *Proc. SPIE* **3889**, 120 (2000).
- [39] J. V. Moloney, R. Indik, J. Hader, and S. Koch, *J. Opt. Soc. Am. B* **16**, 2023 (1999).
- [40] E. Gehrig, O. Hess, C. Ribbat, R. L. Sellin, and D. Bimberg, *Appl. Phys. Lett.* **84**, 1650 (2004).
- [41] D. Rodriguez, I. Esquivias, S. Deubert, J. P. Reithmaier, A. Forchel, M. Krakowski, M. Calligaro, and O. Parillaud, *IEEE J. Quantum Electron.* **41**, 117 (2005).
- [42] G. J. de Valcarcel, E. Roldan, and F. Prati, *Rev. Mex. Fis.* **E52**, 198 (2006).
- [43] G. Tissoni, L. Spinelli, L. A. Lugiato, and M. Brambilla, *Proc. SPIE* **4283**, 577 (2001).
- [44] L. Spinelli, G. Tissoni, L. A. Lugiato, and M. Brambilla, *Phys. Rev. A* **66**, 023817 (2002).
- [45] N. Stelmakh, *IEEE J. Quantum Electron.* **19**, 1392 (2007).
- [46] E. Cabrera, O. G. Calderon, and J. M. Guerra, *Phys. Rev. A* **70**, 063808 (2004).
- [47] J. Mukherjee, Ph.D. thesis, University College, Cork, Ireland, 2009.
- [48] J. Yao, G. P. Agrawal, P. Gallion, and C. M. Bowden, *Opt. Commun.* **119**, 246 (1995).
- [49] J. Martín-Regalado, G. H. M. van Tartwijk, S. Balle, and M. San Miguel, *Phys. Rev. A* **54**, 5386 (1996).
- [50] M. Lax, *Phys. Rev.* **160**, 290 (1967).
- [51] M. Lax, *Phys. Rev.* **157**, 213 (1967).
- [52] D. Meschede, *Optics, Light and Lasers: The Practical Approach to Modern Aspects of Photonics and Laser Physics* (Wiley, New York, 2004), Chap. 8.
- [53] M. San Miguel, Q. Feng, and J. V. Moloney, *Phys. Rev. A* **52**, 1728 (1995).
- [54] M. San Miguel, *Semiconductor Quantum Optoelectronics: from Quantum Physics to Smart Devices*, Proceedings of the 50th Scottish Universities Summer School in Physics, edited by A. Miller, M. Ebrahimzadeh, and D. M. Finlayson (SUSSP, Bristol, 1999).
- [55] M. F. H. Tarroja, N. B. Abraham, D. K. Bandy, and L. M. Narducci, *Phys. Rev. A* **34**, 3148 (1986).
- [56] G. H. M. van Tartwijk and G. P. Agrawal, *Prog. Quantum Electron.* **22**, 43 (1998).
- [57] The choice of sign for $\alpha = \frac{\partial \chi_{\text{Re}} / \partial N}{\partial \chi_{\text{Im}} / \partial N}$ depends on which time factor $e^{\pm i\omega t}$ is chosen to write the dynamical variables E and P in Eqs. (1) and (2), since $\chi(\omega) = \chi^*(-\omega) \Rightarrow \chi_{\text{Re}}(\omega) = \chi_{\text{Re}}(-\omega)$ and $\chi_{\text{Im}}(\omega) = -\chi_{\text{Im}}(-\omega)$ [52]. We use $e^{-i\omega t}$ which means that gain corresponds to $-\chi_{\text{Im}} > 0$ and hence $\alpha > 0$.
- [58] J. Houlihan, J. R. O'Callaghan, V. Voignier, G. Huyet, and J. G. McInerney, *Opt. Lett.* **26**, 1556 (2001).
- [59] M. Clerc, P. Couillet, and E. Tirapegui, *Opt. Commun.* **167**, 159 (1999).
- [60] C. Z. Ning, R. A. Indik, and J. V. Moloney, *IEEE J. Quantum Electron.* **33**, 1543 (1997).
- [61] J. Mukherjee and J. G. McInerney, *Proc. SPIE* **6468**, 64681A (2007).
- [62] A. Markus, J. X. Chen, O. Gauthier-Lafaye, J. G. Provost, C. Paranthoën, and A. Fiore, *IEEE J. Sel. Top. Quantum Electron.* **9**, 1308 (2003).
- [63] P. Mandel, *Theoretical Problems in Cavity Nonlinear Optics* (Cambridge University Press, Cambridge, England, 1997).
- [64] N. B. Abraham, L. A. Lugiato, P. Mandel, L. M. Narducci, and D. K. Bandy, *J. Opt. Soc. Am. B* **2**, 35 (1985).
- [65] M. Brambilla, T. Maggipinto, I. M. Perrini, S. Barbay, and R. Kuszelewicz, *Chaos* **17**, 037119 (2007).
- [66] H. C. Casey, Jr. and M. B. Panish, *Heterostructure Lasers* (Academic, New York, 1978).
- [67] H. Wang, E. T. Aw, M. Xia, M. G. Thompson, R. V. Penty, I. H. White, and A. R. Kovsh, Optical Fiber Conference (unpublished).
- [68] A. V. Uskov, T. W. Berg, and J. Mørk, *IEEE J. Quantum Electron.* **40**, 306 (2004).
- [69] X. Hachair, F. Pedaci, E. Caboche, S. Barland, M. Giudici, J. R. Tredicce, F. Prati, G. Tissoni, R. Kheradmand, L. A. Lugiato, I. Protzenko, and M. Brambilla, *IEEE J. Sel. Top. Quantum Electron.* **12**, 339 (2006).

- [70] S. Balle, *Opt. Commun.* **119**, 227 (1995).
- [71] F. Prati and L. Columbo, *Phys. Rev. A* **75**, 053811 (2007).
- [72] J. Piprek, *Semiconductor Optoelectronic Devices: Introduction to Physics and Simulation* (Academic, New York, 2003).
- [73] P. K. Jakobsen, J. V. Moloney, A. C. Newell, and R. Indik, *Phys. Rev. A* **45**, 8129 (1992).
- [74] U. Bortolozzo, P. Villoresi, and P. L. Ramazza, *Phys. Rev. Lett.* **87**, 274102 (2001).
- [75] S. P. Hegarty, G. Huyet, J. G. McInerney, and K. D. Choquette, *Phys. Rev. Lett.* **82**, 1434 (1999).
- [76] J. Mukherjee and J. G. McInerney, *IEEE J. Sel. Top. Quantum Electron.* **13**, 1180 (2007).
- [77] B. Corbett (private communication).
- [78] H. D. Summers, P. Dowd, I. H. White, and M. R. T. Tan, *IEEE Photon. Technol. Lett.* **7**, 736 (1995).
- [79] P. A. Chen, C. Juang, and C. Y. Chang, *IEEE J. Quantum Electron.* **29**, 2607 (1993).
- [80] H. G. Winful and L. Rahman, *Phys. Rev. Lett.* **65**, 1575 (1990).
- [81] J. LeClech, M. Ziegler, J. Mukherjee, J. W. Tomm, T. Elsaesser, J.-P. Landesman, B. Corbett, J. G. McInerney, J. P. Reithmaier, S. Deubert, A. Forchel, W. Nakwaski, and R. P. Sarzała, *J. Appl. Phys.* **105**, 014502 (2009).
- [82] J. W. Tomm, F. Rinner, J. Rogg, E. Thamm, C. Ribbat, R. Sellin, and D. Bimberg, *Proc. SPIE* **4993**, 91 (2003).
- [83] G. H. M. van Tartwijk and G. P. Agrawal, *Opt. Commun.* **133**, 565 (1997).
- [84] I. V. Babushkin, M. Schulz-Ruhtenberg, N. A. Loiko, K. F. Huang, and T. Ackemann, *Phys. Rev. Lett.* **100**, 213901 (2008).
- [85] T. Rossler, R. A. Indik, G. K. Harkness, J. V. Moloney, and C. Z. Ning, *Phys. Rev. A* **58**, 3279 (1998).
- [86] C. Harder, in *Pump Diode Lasers in Optical Fiber Telecommunications VA: Components and Subsystems*, edited by I. P. Kaminow, T. Li, and A. E. Willner (Academic Press, New York, 2008).
- [87] I. Fischer, T. Burkhard, and W. Elsasser, in *Technical Digest, Summaries of Papers Presented at the Conference of Lasers and Electro-Optics (CLEO), Baltimore, MD, 1999* (Optical Society of America, Washington, D.C., 1999).
- [88] R. Graham and Y. Cho, *Opt. Commun.* **47**, 52 (1983).
- [89] V. S. Idiatulin and A. V. Uspenskii, *Radio Eng. Electron. Phys.* **18**, 422 (1973).
- [90] B. Meziane, *Opt. Quantum Electron.* **30**, 99 (1998).
- [91] B. Meziane, *Phys. Rev. A* **48**, 2346 (1993).
- [92] O. C. Zienkiewicz, R. L. Taylor, and J. Z. Zhu, *The Finite Element Method: Its Basis and Fundamentals*, 6th ed. (Butterworth-Heinemann, Oxford, 2005).
- [93] T. Asatsuma, Y. Takiguchi, S. Frederico, A. Furukawa, and S. Hirata, *Proc. SPIE* **6104**, 105 (2006).
- [94] G. Ropars, M. Vallet, M. Brunel, A. Le Floch, and G. P. Agrawal, *IEEE Photon. Technol. Lett.* **17**, 747 (2005).
- [95] T. Burkhard, I. Fischer, and W. Elsasser, in *Technical Digest, Summaries of Papers Presented at the Conference of Lasers and Electro-Optics (CLEO), Baltimore, MD, 1999* (Optical Society of America, Washington, D.C., 1999), p. 150-151.